



The Chilean GNSS Network: Current Status and Progress toward Early Warning Applications

by J. C. Báez, F. Leyton, C. Troncoso, F. del Campo, M. Bevis, C. Vigny, M. Moreno, M. Simons, E. Kendrick, H. Parra, and F. Blume

ABSTRACT

Chile is one of the world's most seismically active regions and is therefore extensively studied by the earthquake sciences. The great length of the country hosts a variety of measurement systems allowing for the characterization of earthquake processes over a wide range of timescales and in different phases of the seismic cycle. Starting in the early 1990s, several research groups began to deploy continuously operating geodetic networks in Chile, forming the core of the modern network of Global Navigation Satellite Systems (GNSS) receivers used to monitor geodynamics from the southern tip of the Americas to the central Andes. Today, the Centro Sismológico Nacional (CSN) of the Universidad de Chile maintains and improves this network, increasing its coverage and spatial density while greatly reducing solution latency. We present the status of the GNSS network, its data streams, and the real-time analysis system used to support real-time modeling of earthquakes. The system takes 2 s, on average, to collect raw data, estimate positions, and stream results. Such low latency is essential to enabling early warning of earthquakes and tsunamis in Chile.

Electronic Supplement: Figures showing schema of communication from the stations to the servers used at Centro Sismológico Nacional (CSN), comparison between velocities derived from real-time Global Navigation Satellite Systems (RT-GNSS) data, kinematic finite-fault inversion results and waveform comparison, and results of the estimation of M_w as a function of time, and tables of station locations and estimated total coseismic displacement.

INTRODUCTION

Deformation rates of the Earth's surface, derived from modern space geodesy, constitute the observational basis for physical

models of the earthquake deformation cycle, providing key information to describe the processes leading up to and following great events (e.g., Vigny *et al.*, 2011; Ruiz *et al.*, 2014; Schurr *et al.*, 2014; Duputel *et al.*, 2015; Melnick *et al.*, 2017). Along the Chilean subduction zone, the Chilean network of Global Navigation Satellite Systems (GNSS) has been steadily growing from the early 1990s to the present day, with the earliest stations coming from different international research projects and institutions such as the central Andes Global Positioning System (GPS) project (CAP) (Bevis *et al.*, 1999; Kendrick *et al.*, 1999), the German Research Centre for Geosciences (GFZ), the currently active Integrated Plate Boundary Observatory Chile (Angermann *et al.*, 1999; Klotz *et al.*, 2017; Moreno *et al.*, 2017), the French National Research SUBChile project by Institute de Physique du Globe de Paris and École Normale Supérieure in Paris, France (Ruegg *et al.*, 2009; Vigny *et al.*, 2009), and the Central Andean Tectonic Observatory Geodetic Array of the California Institute of Technology (Caltech) (Simons *et al.*, 2010; Bejar-Pizarro *et al.*, 2013).

At the end of the twentieth century, GNSS data from continuous and campaign observations were primarily used in Chile and neighboring countries to estimate plate motion and interseismic deformation (Norabuena *et al.*, 1998; Angermann *et al.*, 1999; Bevis *et al.*, 1999, 2001; Kendrick *et al.*, 1999, 2003, 2006; Brooks *et al.*, 2003; Ruegg *et al.*, 2009; Moreno *et al.*, 2011; Bejar-Pizarro *et al.*, 2013; Metois *et al.*, 2013; Melnick *et al.*, 2017). The GNSS network now provides good spatial coverage throughout Chile's seismogenic zone, enabling the observation of the complete seismic cycle, including the coseismic deformation caused by the M_w 8.8 giant Maule event in 2010 (Vigny *et al.*, 2011; Moreno *et al.*, 2012; Lin *et al.*, 2013), and by events in Iquique (M_w 8.1) in 2014 (Ruiz *et al.*, 2014), Illapel (M_w 8.3) in 2015 (Duputel *et al.*, 2015; Melgar, Crowell, *et al.*, 2015; Ruiz *et al.*, 2016), and Chiloé (M_w 7.4) in 2016 (Melgar *et al.*, 2017; Ruiz, Aden-Antoniow, *et al.*, 2017; Ruiz, Moreno, *et al.*, 2017). The GNSS network also records the postseismic transients caused by these events (Bedford *et al.*, 2013, 2016; Klein *et al.*, 2016). Several researchers proposed the use of real-time GNSS (RT-GNSS) data to estimate not only the magnitude of an event but also its rupture geometry

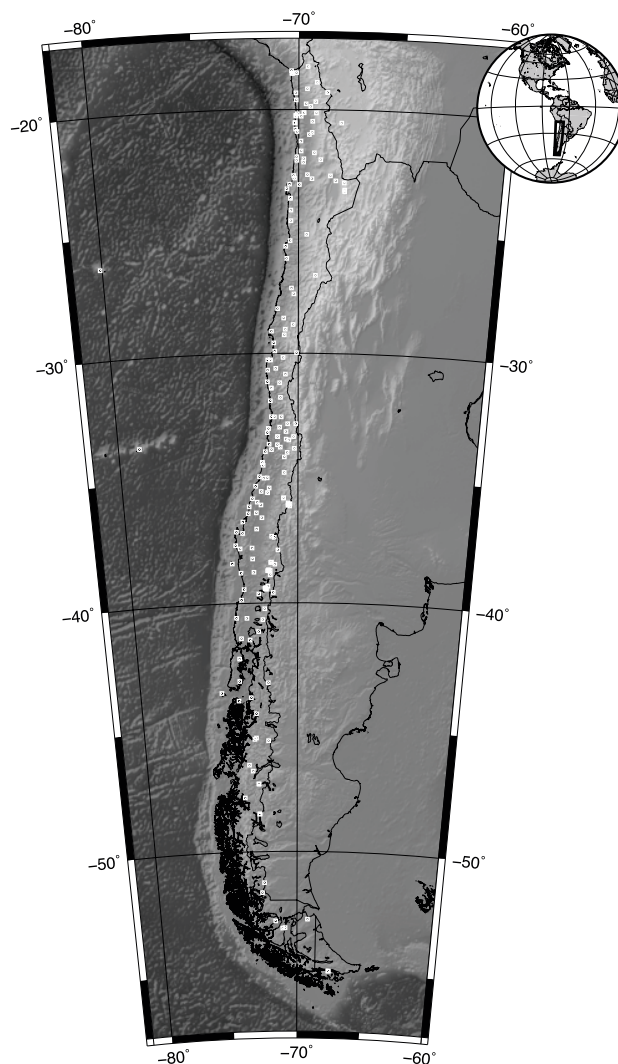
(e.g., GPSlip, Böse *et al.*, 2013; G-larmS, Grapenthin *et al.*, 2014; Bayesian Evidence-based Fault Orientation and Real-time Earthquake Slip, Minson *et al.*, 2014; Geodetic first Approximation of Size and Timing [G-FAST], Crowell *et al.*, 2016). These methods take advantage of the fact that GNSS data do not saturate with magnitude, and directly deliver displacement waveforms, thereby avoiding the serious problems associated with the double integration of accelerograms (Melgar *et al.*, 2013). GNSS data have also been successfully utilized in prototype tsunami early warning systems (Melgar, Allen, *et al.*, 2015; Chen *et al.*, 2016; Riquelme *et al.*, 2016), rapidly inverting for the slip distribution of the earthquake on a pre-defined plate geometry using both GNSS displacement and seismic observations.

Centro Sismológico Nacional's (CSN) current priority is to implement tsunami and earthquake early warning systems in real time. We describe here the status of the GNSS network and the schedule of solutions generated during a rapid response to a moderate-to-large earthquake (magnitude 7.0 and above).

NETWORK ARCHITECTURE

Chile's GNSS network grew most rapidly following the 2010 M_w 8.8 Maule earthquake, when the CAP and Caltech groups joined to build 40 continuous GNSS stations in the immediate aftermath of the earthquake, using financial support from the U.S. National Science Foundation and equipment provided by UNAVCO. From 2013 to the present day, the CSN has deployed an additional 130 stations. These stations either supplement or replace those deployed in the projects listed in the Introduction. The map of all current GNSS stations can be seen in Figure 1 and their codes and locations are given in Table S1, available in the electronic supplement to this article. All the stations observe in continuous mode and 62% stream data to CSN servers. CSN's goal is to increase the number of streams so as to include all available geophysical (GNSS, broadband seismic, or accelerometer) sensors. Data are sent to the CSN servers in one of the following three ways: (1) satellite communication with Intelsat 23 (VSAT), (2) cellular modem 3G/4G into the Internet Cloud (with optical fiber), and (3) wireless link (900 MHz or 5.8 GHz). In some cases, a combination of these communication methods is applied, depending on the specific site conditions (see Fig. S1).

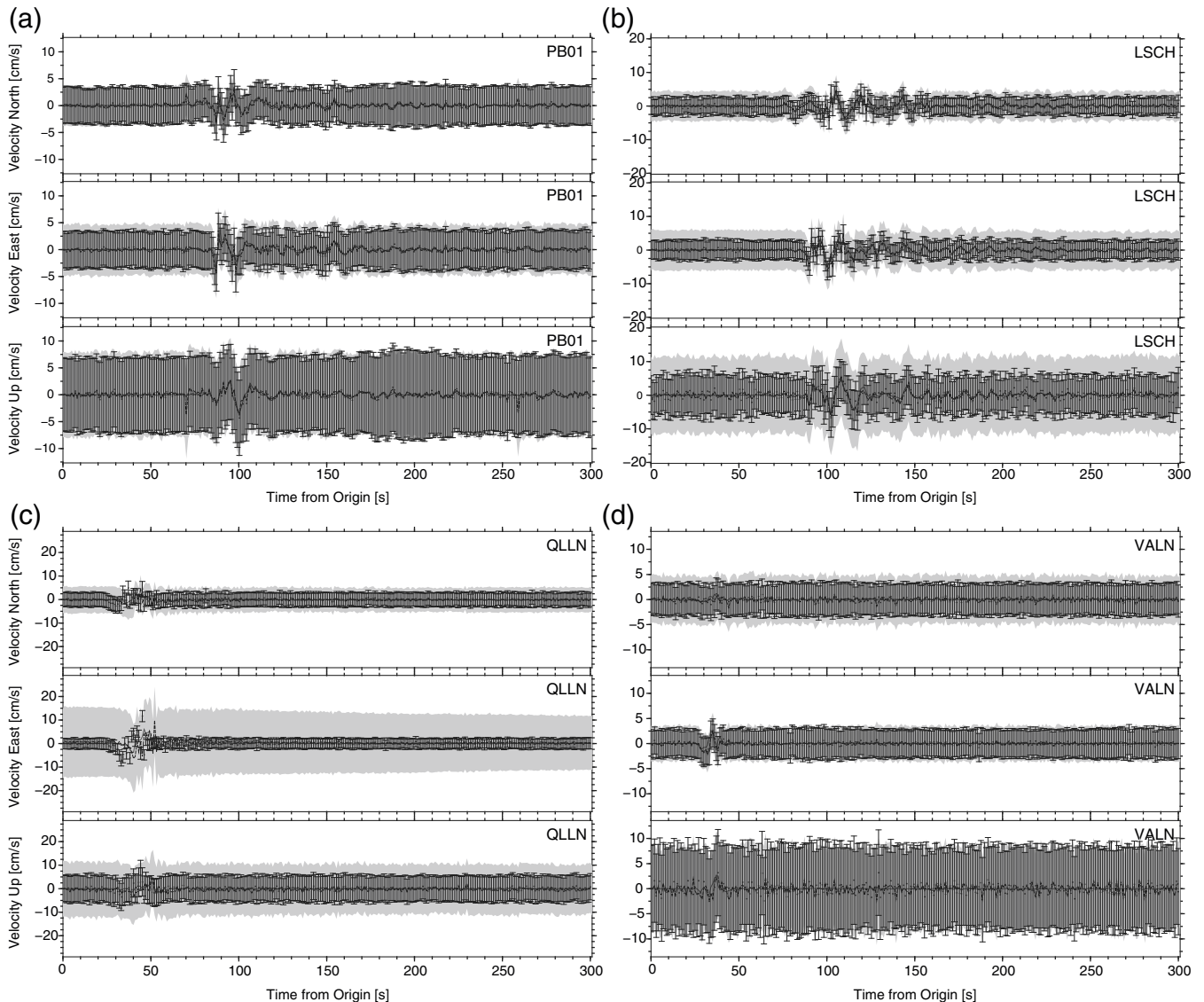
For GNSS data at 1 Hz sampling, we stream the observations using the Radio Technical Commission for Maritime service protocol to an NTRIP Caster (Weber, 2002). At the CSN servers, these observations are processed using a precise point positioning (PPP) approach, including the International GNSS Service (IGS) real-time products (see Data and Resources). For coastal stations located between 18.4° S and 34.5° S we estimate the position on-site using the center point real-time positioning service, a method comparable to PPP (for details, see Glocker *et al.*, 2012), before streaming these positions and respective errors to CSN servers. At the CSN servers, all observations are converted into a 15-s RINEX format (Gurtner



▲ **Figure 1.** Maps showing the distribution of Global Navigation Satellite Systems (GNSS) stations (white squares). The inset shows the location of the study region in South America.

and Estey, 2005) that are stored and published on an ftp server (see Data and Resources for details). CSN is currently using these data to produce daily solutions for several research efforts beyond the scope of early warning such as plate boundary and fault segmentation, locking rates, and interseismic straining (e.g., Bedford *et al.*, 2013, 2016; Klein *et al.*, 2016). In the following section, we will focus on the RT-GNSS products that are currently being used in the study of moderate-to-large earthquakes (magnitude 7.0 and above).

Currently, we are working on the implementation of a new system that is able to observe collocated displacement and acceleration (Minson *et al.*, 2014). At each station, a smartphone generates smoothed position estimates derived from a single-frequency GNSS chip plus a three-component acceleration time series obtained from internal accelerometers. The idea of this system is to quickly detect an earthquake and then estimate its magnitude and location, similar to more conven-



▲ **Figure 2.** A comparison between velocities derived from real-time (RT)-GNSS data, obtained from precise point positioning (PPP) with corrected orbits and the ambiguities resolution (AP) with final orbits solutions (PPP-AR), shown in black dots and dashed lines, respectively. The corresponding errors are shown with vertical bars (PPP-AR) and gray shading (for PPP). Dark gray line show strong-motion data (ACC), when available. Data belong to the following stations and events: (a) PB01 for the 2014 M_w 8.1 Iquique, (b) LSCH for the 2015 M_w 8.3 Illapel, (c) QLLN for the 2016 M_w 7.6 Chiloé, and (d) VALN for the 2017 M_w 6.9 Valparaíso. Note the comparisons are made in velocity, for the three components. The color version of this figure is available only in the electronic edition.

tional early warning systems (Allen *et al.*, 2009). Deployment was largely completed in 2017, and we expect to have an operational system in 2018.

RT-GNSS PRODUCTS AND THEIR APPLICATION TO SEISMOLOGY

Validation of RT-GNSS Products

The real-time positioning streams are monitored as continuous time series, so that the variation of position and respective errors can be clearly visualized. From these time series, we recover ground position, estimate peak ground displacement, derive

ground velocity, and recover the static displacement due to moderate-to-large earthquakes (magnitude 7.0 and above). We tested the results obtained from RT-GNSS (the PPP solutions) by comparing them with strong-motion records (ACC) and PPP with ambiguity resolution (PPP-AR), using final orbits for recent events, as shown in Figure 2. PPP-AR solutions have a 15-day latency. Both GNSS time series (PPP and PPP-AR) are converted into velocity by differentiating, point by point, in the time domain. For the strong-motion records, for each trace, we first remove the trend, in the time domain, and then the instrumental response, in the frequency domain. We then integrate to obtain velocities in the time domain before applying a Butter-

Table 1 Results of the Cross Correlation between Real-Time Global Navigation Satellite Systems Data Determined Using Precise Point Position (PPP) Using Corrected Orbits and PPP with Ambiguities Resolution (AR) Using Final Orbits (PPP-AR), Strong-Motion Records (ACC) for All Available Stations for the Following Events: 2014 M_w 8.1 Iquique, 2015 M_w 8.4 Illapel, 2016 M_w 7.6 Chiloé, and 2017 M_w 6.9 Valparaíso				
Event	Component			N Stations
	North–South	East–West	Up	
PPP versus PPP-AR				
2014 Iquique	0.84	0.85	0.80	14
2015 Illapel	0.82	0.89	0.77	13
2016 Chiloé	0.62	0.64	0.64	5
2017 Valparaíso	0.66	0.73	0.64	7
PPP versus ACC				
2014 Iquique	0.66	0.63	0.63	9
2015 Illapel	0.67	0.65	0.64	3
2016 Chiloé	0.66	0.64	0.63	1
2017 Valparaíso	0.62	0.61	0.63	2

We show the average results for each component (north–south, east–west, and up) and the number of stations considered in each case.

worth low-pass filter at 0.5 Hz. Figure 2 also shows the errors estimated at each point, shown in gray area for PPP and vertical bars for PPP-AR. Error magnitudes are generally comparable for PPP and PPP-AR solutions but there are notable error reductions in PPP-AR solutions for QLLN east–west and vertical components (Fig. 2c, middle and lower panels) and LSCH vertical component (Fig. 2b, lower panel). These comparisons are made for velocities (transformed from errors in displacement). The time series of PPP (dashed lines) and PPP-AR (black dots) show clear similarities, with the PPP having greater scatter than the PPP-AR time series, due to the differences in the used orbits (corrected vs. final). Additionally, we can see the similarities between the GNSS and strong-motion data (ACC) for velocity time series despite the high-frequency noise observed in the GNSS PPP data. To quantify the possible differences of PPP with respect to PPP-AR and ACC, we computed the cross correlation for all available traces, as shown in Table 1 (see caption for details). From this table, we see high correlations (always above 0.6) for all cases. For the comparison between PPP and PPP-AR (Table 1), east–west components show better performance, whereas up component, in general, presents smaller correlation coefficients. This could be due to the fact that the vertical component of GNSS is intrinsically noisier than the horizontal components. For the comparison between PPP and ACC, the north–south component gives the strongest correlation, with the up component showing the weakest correlation coefficient. We believe that these results demonstrate the suitability of RT-GNSS data for studies that require displacement waveforms. Results for all available GNSS stations for each of the events are shown in © Figure S2a–d.

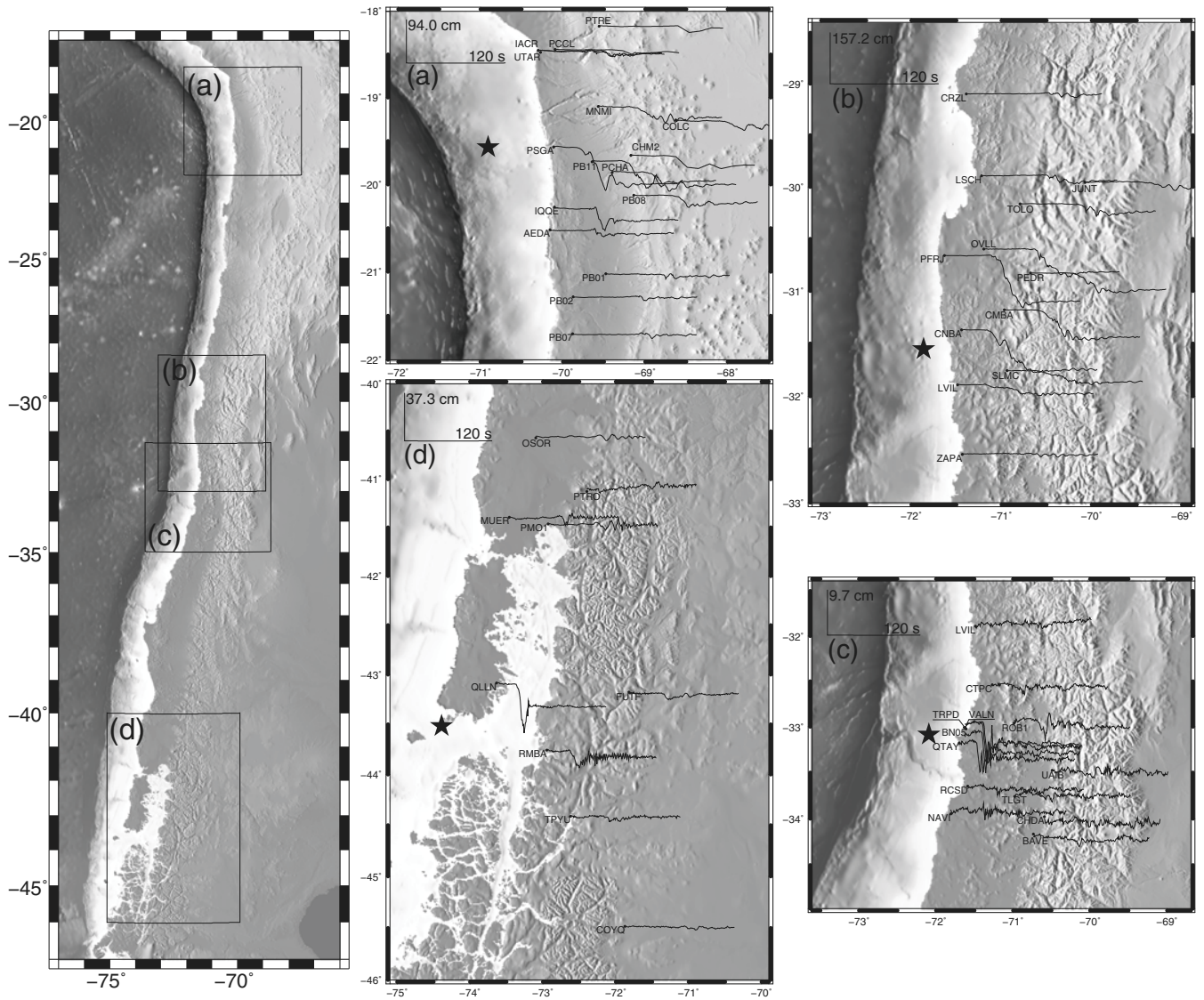
Application to Seismology

Figure 3 shows the east–west component of displacement for all GNSS stations located near the epicentral area for the following events: (a) 2014 M_w 8.1 Iquique, (b) 2015 M_w 8.3 Illapel, (c) 2017 M_w 6.9 Valparaíso, and (d) 2016 M_w 7.4 Chiloé. In this figure, the upper left corner of each panel shows a scale indicating the relative size of the displacement (vertical axis) and the time scale (horizontal axis). A black star shows the location of the epicenter, see figure caption for more details. All displayed traces in Figure 3 were processed in the same way: displacements were computed with respect to the average position 10 min before the origin time of each event. Recently, Riquelme *et al.* (2016) used these data to determine magnitudes and focal mechanisms from large earthquakes in Chile ($M_w \geq 8.0$), using these data to retrieve the W phase. We tested a simple kinematic inversion considering the elliptical patches method (Leyton *et al.*, 2018) for the 2014 M_w 8.1 Iquique earthquake, successfully estimating a finite-fault plane (considering a single ellipse), the moment magnitude, and focal mechanism, as shown in

© Figure S3. In this figure, we also show the radial components of the RT-GNSS (black) and predicted (blue) traces for the considered stations. From these results, we believe that the use of RT-GNSS time series will play a key role in the rapid characterization of future large earthquakes, potentially giving crucial information for early warning systems.

From displacement time series, Melgar, Crowell, *et al.* (2015) have shown that the peak ground displacement enables a fast and robust estimation of magnitude, given an approximate location of the hypocenter. Furthermore, Melgar, Allen, *et al.* (2015) and Crowell *et al.* (2016) implemented these estimations in early warning systems such as G-FAST, and successfully applied these systems to Chile (Crowell *et al.*, 2018). We reproduced part of their results for the same set of events previously shown in this article and found that, within the first 60–90 s from the origin time, we obtain an estimation of the magnitude with error of less than 0.3 (see © Fig. S4). Considering these results, it is clear that the tested methodology has great potential for early warning applications (Melgar, Allen, *et al.*, 2015; Melgar, Crowell, *et al.*, 2015; Crowell *et al.*, 2016, 2018).

Finally, we estimate the coseismic static offset at each station produced by the earthquake (as shown in Fig. 4). These data have been extensively used to retrieve source parameters such as the slip distribution and moment magnitude (Moreno *et al.*, 2012; Ruiz *et al.*, 2014, 2016; Ruiz, Aden-Antoniow, *et al.*, 2017; Ruiz, Moreno, *et al.*, 2017); Figure 4 shows results of the slip distribution for the selected events (see figure caption for details). Note the changes in scale in each panel, ranging from centimeter deformations (panel (a) and (b) for magnitudes 7.7 and 6.9, for 2007 Tocopilla and 2017 Valparaíso earthquakes, respectively), up to several meters (central

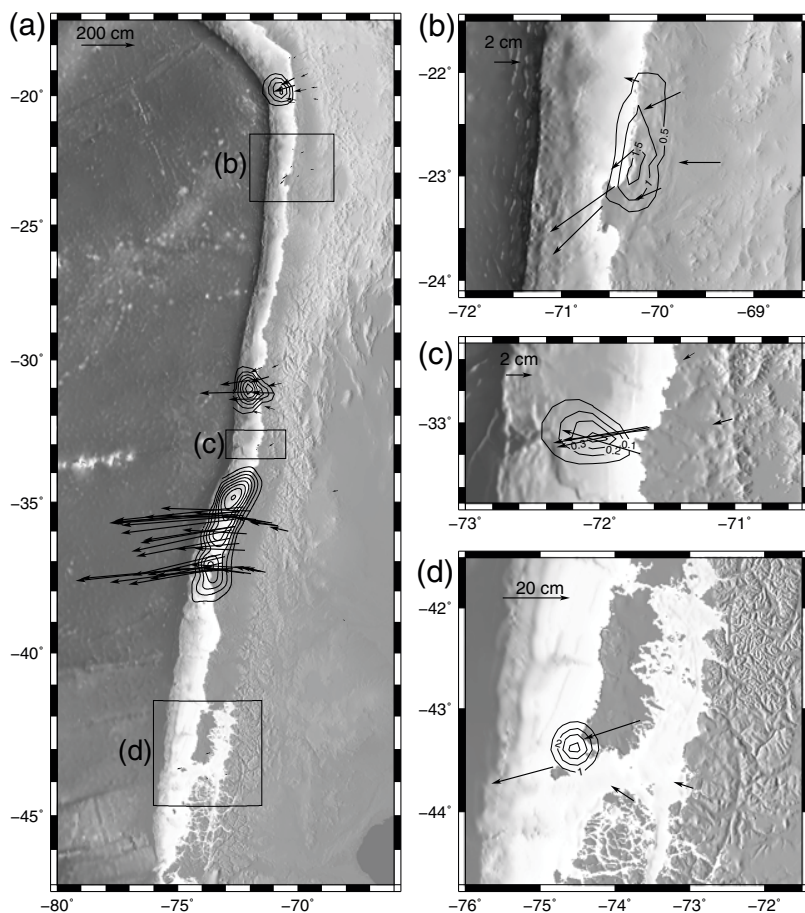


▲ **Figure 3.** Example of GNSS result (east–west component) coming from PPP-AR solution for the following earthquakes: (a) 2014 M_w 8.1 Iquique, (b) 2015 M_w 8.3 Illapel, (c) 2017 M_w 6.9 Valparaíso, and (d) 2016 7.4 Chiloé. In each panel, the black star shows the location of the epicenter, while in the upper left corner is a scale of the displacement and time used.

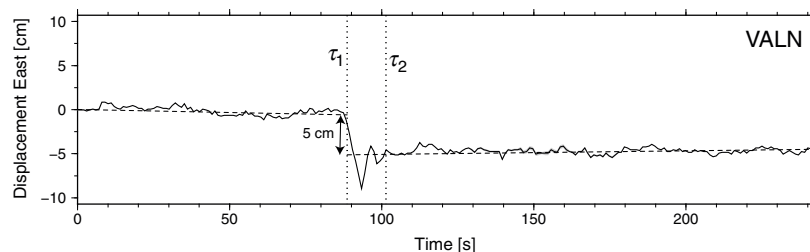
panel for the 2010 M_w 8.8 Maule earthquake). Slip distributions from coseismic static offsets can be determined within the first few minutes after the origin time, and are therefore another tool for early warning applications for moderate-to-large events (magnitudes 7.0 and above). We also tested the static offset results by comparing RT-GNSS data (PPP) with the better derivations that use final orbits (PPP-AR) (as shown in Table S2). Table S2 shows the coseismic static offset of both methods ($|PPP|$ and $|PPP-AR|$), estimated using the methodology described below; the root mean square (rms) of the difference between PPP and PPP-AR, along with the percentage difference with respect to the absolute value ($|PPP-AR|$ in Table S2). Finally, we compute the average coseismic offset and estimate the moment magnitude (M_w), as done in previous studies (Ruiz *et al.*, 2014, 2016; Ruiz, Aden-

Antoniow, *et al.*, 2017; Ruiz, Moreno, *et al.*, 2017) for both estimations (PPP and PPP-AR). As seen for the RT-GNSS velocity time-series results (see the RT-GNSS Products and Their Application to Seismology section), even though we find differences between these two estimations, we believe that the results obtained from RT-GNSS data (PPP) can be successfully applied to the study of moderate-to-large earthquakes.

To recover the coseismic static offset, we identified the epoch τ_1 of the onset of deformation at each station (following Psimoulis *et al.*, 2013), using a sliding window of 60 s for the average (μ) and standard deviation (σ); τ_1 will be defined as the epoch when the ratio between the corrected displacement (removing μ) over σ exceeds a threshold parameter $k = 3$ (see Psimoulis *et al.*, 2013, for details). The end of the main transient was defined as the epoch τ_2 , at which σ



▲ **Figure 4.** (a) Coseismic displacement estimated for the following earthquakes, from north to south: 2014 M_w 8.1 Iquique; 2007 M_w 7.8 Tocopilla, zoomed in (b); 2015 M_w 8.4 Illapel; 2017 M_w 6.9 Valparaíso, zoomed in (c); 2010 M_w 8.8 Maule; and 2016 M_w 7.6 Chiloé, zoomed in (d). Note the change in scale for each panel shown in the upper left corner. We also present the results of slip distributions (contour lines) estimated from these data by [Moreno *et al.* \(2012\)](#), [Ruiz *et al.* \(2014, 2016\)](#), [Ruiz, Aden-Antoniow, *et al.* \(2017\)](#), and [Ruiz, Moreno, *et al.* \(2017\)](#). Contour lines are plotted every 1 m, except for 2010 Maule that is plotted every 2 m, 2007 Tocopilla plotted every 0.5 m (b), and 2017 Valparaíso plotted every 0.1 m (d).



▲ **Figure 5.** An example of estimation of coseismic displacement for the 2017 M_w 6.9 Valparaíso event at station VALN. We also show the location of the epoch τ_1 and τ_2 . Note that 5 cm displacement to the west was successfully retrieved for this event.


diminished to three times its value at the detection onset. To retrieve the static offsets, we performed least-squares linear regressions in windows of 15 min, one just before τ_1 and another immediately after τ_2 and evaluated the difference between the linear trends at τ_1 . An example is shown in Figure 5, where a 5 cm displacement to the west was successfully retrieved for the 2017 M_w 6.9 Valparaíso event at station VALN; this figure shows the location of the epoch τ_1 and τ_2 described above.

FINAL COMMENTS

Many of the most exciting discoveries in subduction zone phenomenology during the last two decades have precipitated from the increased spatial density of continuously operating GNSS networks. We believe that such density increase will also benefit earthquake and tsunami early warning systems. In this study, we presented the state-of-the-art methods and products of the Chilean GNSS network, managed by CSN, with focus on the applications to real-time detection of coseismic deformation and rapid response capabilities for moderate-to-large earthquakes. GNSS data and modeling present two main advantages over traditional seismic products: (1) GNSS solutions do not saturate with magnitude; and (2) GNSS provides waveforms directly in displacement, avoiding the known problems of double integration of accelerograms. Currently, considerable resources are being devoted to testing and developing methodologies that rapidly provide useful and robust information for moderate-to-large earthquakes (magnitude 7.0 and above) using the RT-GNSS data.

In general, all CSN GNSS stations are analyzed using PPP software to produce continuous streams of positioning. Some of them work at each receiver, using correction products obtained from satellites, taking less than 1 s, on average, to arrive at the acquisition system. At other stations, the observations are streamed to CSN servers, where the PPP, including IGS corrections of orbit and clock, is performed. This data procedure takes 2 s, on average, to estimate and stream the results from the acquisition system. We do not believe that these time lags represent a significant delay to the rapid-response methodologies presented in this study. Therefore, real-time high-rate GNSS of the CSN network currently provides useful information to rapidly extract the static offset of earthquakes and to assess their seismic hazard.

DATA AND RESOURCES

All data used here were provided by Centro Sismológico Nacional (CSN) of the Universidad de Chile and can be retrieved from the Global Navigation Satellite Systems (GNSS) database (<http://gps.csn.uchile.cl>, last accessed June 2017). The other information about International GNSS Service (IGS) can be found at <http://www.igs.org/rts/products> (last accessed February 2018). 

ACKNOWLEDGMENTS

The authors would like to thank the Chilean National Science Foundation Fondo Nacional de Desarrollo Científico y Tecnológico (FONDECYT) projects Numbers 1151175, 1170430, and 1181479, and the Centro Sismológico Nacional (CSN) of the Universidad de Chile for maintenance, operation, and the open data policy. The authors acknowledge the valuable contribution of LIA 'Montessus de Ballore' International Laboratory to the development of Global Navigation Satellite Systems (GNSS) studies in Chile. The authors also thank the U.S. National Science Foundation for funding the central Andes Global Positioning System (GPS) Project. All figures were made using Generic Mapping Tool (GMT) software (Wessel *et al.*, 2013).

REFERENCES

- Allen, R. M., P. Gasparini, O. Kamigaichi, and M. Böse (2009). The status of earthquake early warning around the world: An introductory overview, *Seismol. Res. Lett.* **80**, no. 5, 682–693, doi: [10.1785/SSRL80.5.682](https://doi.org/10.1785/SSRL80.5.682).
- Angermann, D., J. Klotz, and C. Reigber (1999). Space-geodetic estimations of the Nazca-South America Euler vector, *Earth Planet. Sci. Lett.* **171**, 329–334, doi: [10.1016/S0012-821X\(99\)00173-9](https://doi.org/10.1016/S0012-821X(99)00173-9).
- Bedford, J., M. Moreno, J. C. Báez, D. Lange, F. Tilmann, M. Rosenau, O. Heidbach, O. Oncken, M. Bartsch, A. Rietbrock, *et al.* (2013). A high-resolution, time-variable afterslip model for the 2010 Maule M_w 8.8, Chile megathrust earthquake, *Earth Planet. Sci. Lett.* **383**, doi: [10.1016/j.epsl.2013.09.020](https://doi.org/10.1016/j.epsl.2013.09.020).
- Bedford, J., M. Moreno, S. Li, O. Oncken, J. C. Baez, M. Bevis, O. Heidbach, and D. Lange (2016). Separating rapid relocking, afterslip, and viscoelastic relaxation: An application of the postseismic straightening method to the Maule 2010 cGPS, *J. Geophys. Res.* **121**, no. 10, 7618–7638, doi: [10.1002/2016JB013093](https://doi.org/10.1002/2016JB013093).
- Bejar-Pizarro, M., A. Socquet, R. Armijo, D. Carrizo, J. Genrich, and M. Simons (2013). Andean structural control on interseismic coupling in the North Chile subduction zone, *Nature Geosci.* **6**, 462–467, doi: [10.1038/NGEO1802](https://doi.org/10.1038/NGEO1802).
- Bevis, M., E. Kendrick, R. Smalley, B. Brooks, R. Allmendinger, and B. Isacks (2001). On the strength of interplate coupling and the rate of backarc convergence in the central Andes: An analysis of the interseismic velocity field, *Geochem. Geophys. Geosys.* **2**, no. 11, doi: [10.1029/2001GC000198](https://doi.org/10.1029/2001GC000198).
- Bevis, M., E. Kendrick, R. Smalley, T. Herring, J. Godoy, and F. Galban (1999). Crustal motion north and south of the Arica deflection: Comparing recent geodetic results from the Central Andes, *Geochem. Geophys. Geosys.* **1**, no. 12, doi: [10.1029/1999GC000011](https://doi.org/10.1029/1999GC000011).
- Böse, M., T. H. Heaton, and K. W. Hudnut (2013). Combining real-time seismic and GPS data for earthquake early warning, *AGU Fall Meeting Abstracts*, #G51B-05, available at <http://adsabs.harvard.edu/abs/2013AGUFM.G51B..05B> (last accessed April 2018).
- Brooks, B., M. Bevis, R. Smalley, E. Kendrick, R. Manceda, E. Lauría, R. Maturana, and M. Araujo (2003). Crustal motion in the Southern Andes (26°S–36°S): Do the Andes behave like a microplate? *Geochem. Geophys. Geosys.* **4**, no. 10, 1085, doi: [10.1029/2003GC000505](https://doi.org/10.1029/2003GC000505).
- Chen, K., A. Babeyko, A. Hoehner, and M. Ge (2016). Comparing source inversion techniques for GPS-based local tsunami forecasting: A case study for the April 2014 M_w 8.1, Iquique, Chile, earthquake, *Geophys. Res. Lett.* **43**, no. 7, 3186–3192, doi: [10.1002/2016GL068042](https://doi.org/10.1002/2016GL068042).
- Crowell, B. W., D. A. Schmidt, P. Bodin, J. E. Vidale, B. Baker, S. Barrientos, and J. Geng (2018). G-FAST earthquake early warning potential for great earthquakes in Chile, *Seismol. Res. Lett.* **89**, 542–556, doi: [10.1785/0220170180](https://doi.org/10.1785/0220170180).
- Crowell, B. W., D. A. Schmidt, P. Bodin, J. E. Vidale, J. Gombert, J. R. Hartog, V. C. Kress, T. I. Melbourne, M. Santillan, S. E. Minson, *et al.* (2016). Demonstration of the Cascadia G-FAST geodetic earthquake early warning system for the Nisqually, Washington, earthquake, *Seismol. Res. Lett.* **87**, no. 4, 930–943, doi: [10.1785/0220150255](https://doi.org/10.1785/0220150255).
- Duputel, Z., J. Jiang, R. Jolivet, M. Simons, L. Rivera, J. P. Ampuero, B. Riel, S. Owen, A. W. Moore, S. V. Samsonov, *et al.* (2015). The Iquique earthquake sequence of April 2014: Bayesian modeling accounting for prediction uncertainty, *Geophys. Res. Lett.* **42**, no. 19, 7949–7957, doi: [10.1002/2015GL065402](https://doi.org/10.1002/2015GL065402).
- Glocker, M., H. Landau, R. Leandro, and M. Nitschke (2012). Global precise multi-GNSS positioning with Trimble CenterPoint RTX, *European Workshop on GNSS Signal Processing*, doi: [10.1109/NAVITEC.2012.6423060](https://doi.org/10.1109/NAVITEC.2012.6423060).
- Grapenthin, R., I. A. Johanson, and R. M. Allen (2014). Operational real-time GPS-enhanced earthquake early warning, *J. Geophys. Res.* **19**, no. 10, 7944–7965, doi: [10.1002/2014JB011400](https://doi.org/10.1002/2014JB011400).
- Gurtner, W., and L. Estey (2005). *RINEX: The Receiver Independent Exchange Format Version 2.11*, available at <http://nptel.ac.in/courses/105107062/module8/lecture4/AppendixA.pdf> (last accessed April 2018).
- Kendrick, E., M. Bevis, R. Smalley, B. Brooks, R. Barriga, E. Lauría, and L. P. S. Fortes (2003). The Nazca–South America Euler vector and its rate of change, *J. S. Am. Earth Sci.* **16**, 125–131, doi: [10.1016/S0895-9811\(03\)00028-2](https://doi.org/10.1016/S0895-9811(03)00028-2).
- Kendrick, E., M. Bevis, R. Smalley, O. Cifuentes, and F. Galban (1999). Current rates of convergence across the Central Andes: Estimates from continuous GPS observations, *Geophys. Res. Lett.* **26**, no. 5, 541–544, doi: [10.1029/1999GL900040](https://doi.org/10.1029/1999GL900040).
- Kendrick, E., B. Brooks, M. Bevis, R. Smalley Jr., E. Lauria, M. Araujo, and H. Parra (2006). Active orogeny of the south-central Andes studied with GPS geodesy, *Rev. Asoc. Geol. Argentina* **61**, 555–566, available at <http://www.scielo.org.ar/img/revistas/raga/v61n4/html/v61n4a10.htm> (last accessed April 2018).
- Klein, E., L. Fleitout, C. Vigny, and J. D. Garau (2016). Afterslip and viscoelastic relaxation model inferred from the large scale postseismic deformation following the 2010 M_w 8.8 Maule earthquake (Chile), *Geophys. J. Int.* **205**, no. 3, 1455–1472, doi: [10.1093/gji/ggw086](https://doi.org/10.1093/gji/ggw086).
- Klotz, J., Z. Deng, M. Moreno, G. Ash, M. Martsch, and M. Ramaschi (2017). Continuous mode GPS data in the IPOC region, northern Chile, *GFZ Data Service*, doi: [10.5880/GFZ.1.1.2017.001](https://doi.org/10.5880/GFZ.1.1.2017.001).
- Leyton, F., S. Ruiz, and R. Madariaga (2018). Focal mechanism, magnitude, and finite-fault rapid estimation using the elliptical patch method in Chile, *Seismol. Res. Lett.* **89**, 503–511, doi: [10.1785/0220170174](https://doi.org/10.1785/0220170174).
- Lin, Y., A. Sladen, F. Ortega-Culaciati, M. Simons, J. F. Avouac, E. Fielding, B. Brooks, M. Bevis, J. Genrich, A. Rietbrock, *et al.* (2013). Coseismic and postseismic slip associated with 2010 Maule earthquake, Chile: Characterizing the Arauco Peninsula barrier effect, *J. Geophys. Res.* **118**, no. 6, 3142–3159, doi: [10.1002/jgrb.50207](https://doi.org/10.1002/jgrb.50207).
- Melgar, D., R. M. Allen, S. Riquelme, J. Geng, F. Bravo, J. C. Báez, H. Parra, S. Barrientos, P. Fang, Y. Bock, *et al.* (2015). Local tsunami warnings: Perspectives from recent large events, *Geophys. Res. Lett.* **43**, no. 3, 1109–1117, doi: [10.1002/2015GL067100](https://doi.org/10.1002/2015GL067100).

- Melgar, D., Y. Bock, D. Sanchez, and B. W. Crowell (2013). On robust and reliable automated baseline corrections for strong motion seismology, *J. Geophys. Res.* **118**, no. 3, 1177–1187, doi: [10.1002/jgrb.50135](https://doi.org/10.1002/jgrb.50135).
- Melgar, D., B. W. Crowell, J. Geng, R. M. Allen, Y. Bock, S. Riquelme, E. M. Hill, M. Protti, and A. Ganas (2015). Earthquake magnitude calculation without saturation from the scaling of peak ground displacement, *Geophys. Res. Lett.* **42**, no. 13, 5197–5205, doi: [10.1002/2015GL064278](https://doi.org/10.1002/2015GL064278).
- Melgar, D., S. Riquelme, X. Xu, J. C. Báez, J. Geng, and M. Moreno (2017). The first since 1960: A large event in the Valdivia segment of the Chilean Subduction Zone, the 2016 M 7.6 Melinka earthquake, *Earth Planet. Sci. Lett.* **474**, 68–75, doi: [10.1016/j.epsl.2017.06.026](https://doi.org/10.1016/j.epsl.2017.06.026).
- Melnick, D., M. Moreno, J. Quinteros, J. C. Báez, Z. Deng, S. Li, and O. Oncken (2017). The super-interseismic phase of the megathrust earthquake cycle in Chile, *Geophys. Res. Lett.* **44**, no. 2, doi: [10.1002/2016GL071845](https://doi.org/10.1002/2016GL071845).
- Metois, M., A. Socquet, C. Vigny, D. Carrizo, S. Peyrat, A. Delorme, E. Maureira, M.-C. Valderas-Bermejo, and I. Ortega (2013). Revisiting the North Chile seismic gap segmentation using GPS-derived interseismic coupling, *Geophys. J. Int.* **194**, no. 3, doi: [10.1093/gji/ggt183](https://doi.org/10.1093/gji/ggt183).
- Minson, S. E., M. Simons, J. L. Beck, F. Ortega, J. Jiang, S. E. Owen, A. W. Moore, A. Inbal, and A. Sladen (2014). Bayesian inversion for finite fault earthquake source models II—The 2011 great Tohoku-Oki, Japan earthquake, *Geophys. J. Int.* **198**, no. 2, 922–940, doi: [10.1093/gji/ggu170](https://doi.org/10.1093/gji/ggu170).
- Moreno, M., J. Bedford, J. C. Báez, J. Klotz, F. Hoffmann, Z. Deng, I. Urrutia, C. Rojas, M. Shrivastava, F. Ortega-Culaciati, et al. (2017). Survey mode GPS data in the IPOC region, Central Andes, Chile, *GFZ Data Service*, doi: [10.5880/GFZ.4.1.2017.003](https://doi.org/10.5880/GFZ.4.1.2017.003).
- Moreno, M., D. Melnick, M. Rosenau, J. C. Báez, J. Klotz, O. Oncken, A. Tassara, J. P. Chen, K. Bataille, M. Bevis, et al. (2012). Toward understanding tectonic control on the M_w 8.8 2010 Maule Chile earthquake, *Earth Planet. Sci. Lett.* **321/322**, 152–165, doi: [10.1016/j.epsl.2012.01.006](https://doi.org/10.1016/j.epsl.2012.01.006).
- Moreno, M., D. Melnick, M. Rosenau, J. Bolte, J. Klotz, H. Ehtler, J. C. Báez, K. Bataille, J. Chen, M. Bevis, et al. (2011). Heterogeneous plate locking in south-central Chile subduction zone: Building up the next great earthquake, *Earth Planet. Sci. Lett.* **305**, nos. 3/4, 413–424, doi: [10.1016/j.epsl.2011.03.025](https://doi.org/10.1016/j.epsl.2011.03.025).
- Norabuena, E., L. Leffler-Griffin, A. Mao, T. Dixon, S. Stein, S. Sacks, L. Ocola, and M. Ellis (1998). Space geodetic observations of Nazca–South America convergence across the central Andes, *Science* **279**, no. 5349, 358–362, doi: [10.1126/science.279.5349.358](https://doi.org/10.1126/science.279.5349.358).
- Psimoulis, P., M. Meindl, N. Houlié, and M. Rothacher (2013). Development of an algorithm for the detection of seismic events based on GPS records: Case study Tohoku-Oki earthquake, *European Geosciences Union General Assembly 2013*, Vienna, Austria, 8–12 April.
- Riquelme, S., F. Bravo, D. Melgar, R. Benavente, J. Geng, S. Barrientos, and J. Campos (2016). W phase source inversion using high-rate regional GPS data for large earthquakes, *Geophys. Res. Lett.* **43**, no. 7, 3178–3185, doi: [10.1002/2016GL068302](https://doi.org/10.1002/2016GL068302).
- Ruegg, J. C., A. Rudloff, C. Vigny, R. Madariaga, J. B. Chabaliér, J. Campos, E. Kausel, S. Barrientos, and D. Dimitrov (2009). Interseismic strain accumulation measured by GPS in the seismic gap between Constitución and Concepción in Chile, *Phys. Earth Planet. In.* **175**, nos. 1/2, 78–85, doi: [10.1016/j.pepi.2008.02.015](https://doi.org/10.1016/j.pepi.2008.02.015).
- Ruiz, S., F. Aden-Antoniow, J. C. Baez, C. Otarola, B. Potin, F. Campo, P. Poli, C. Flores, C. Satriano, F. Leyton, et al. (2017). Nucleation phase and dynamic inversion of the M_w 6.9 Valparaíso 2017 earthquake in Central Chile, *Geophys. Res. Lett.* **44**, no. 20, doi: [10.1002/2017GL075675](https://doi.org/10.1002/2017GL075675).
- Ruiz, S., E. Klein, F. Del-Campo, E. Rivera, P. Poli, M. Metois, C. Vigny, J. C. Báez, G. Vargas, F. Leyton, et al. (2016). The seismic sequence of the September 2015 M_w 8.3 Illapel, Chile, earthquake, *Seismol. Res. Lett.* **87**, no. 4, 789–799, doi: [10.1785/0220150281](https://doi.org/10.1785/0220150281).
- Ruiz, S., M. Metois, A. Fuenzalida, J. Ruiz, F. Leyton, C. Vigny, R. Madariaga, and J. Campos (2014). Intense foreshocks and a slow slip event preceded the 2014 Iquique M_w 8.1 earthquake, *Science* **345**, no. 6201, 1165–1169, doi: [10.1126/science.1256074](https://doi.org/10.1126/science.1256074).
- Ruiz, S., M. Moreno, D. Melnick, F. Del Campo, P. Poli, J. C. Báez, F. Leyton, and R. Madariaga (2017). Reawakening of large earthquakes in south central Chile: The 2016 M_w 7.6 Chiloé event, *Geophys. Res. Lett.* **44**, no. 12, 6633–6640, doi: [10.1002/2017GL074133](https://doi.org/10.1002/2017GL074133).
- Schurr, B., G. Asch, S. Hainzl, J. Bedford, A. Hoechner, M. Palo, R. Wang, M. Moreno, M. Bartsch, Y. Zhang, et al. (2014). Gradual unlocking of plate boundary controlled initiation of the 2014 Iquique earthquake, *Nature* **512**, 299–302, doi: [10.1038/nature13681](https://doi.org/10.1038/nature13681).
- Simons, M., J. Galetzka, J. Genrich, F. Ortega, D. Comte, B. Glass, G. Gonzalez, and E. Norambuena (2010). Central Andean tectonic observatory geodetic array, *UNAVCO. GPS Data Set*, doi: [10.7283/T50P0X37](https://doi.org/10.7283/T50P0X37).
- Vigny, C., A. Rudloff, J. C. Ruegg, R. Madariaga, J. Campos, and M. Alvarez (2009). Upper plate deformation measured by GPS in the Coquimbo gap, Chile, *Phys. Earth Planet. In.* **175**, nos. 1/2, 86–95, doi: [10.1016/j.pepi.2008.02.013](https://doi.org/10.1016/j.pepi.2008.02.013).
- Vigny, V., A. Socquet, S. Peyrat, J. C. Ruegg, M. Métois, R. Madariaga, S. Morvan, M. Lancieri, R. Lacassin, J. Campos, et al. (2011). The 2010 M_w 8.8 Maule mega-thrust earthquake of central Chile, monitored by GPS, *Science* **332**, no. 6036, 1417–1421, doi: [10.1126/science.1204132](https://doi.org/10.1126/science.1204132).
- Weber, G. (2002). Echtzeit-Übertragung von RTCM-Daten über Internet und Mobilfunk, *Beitrag zum 57. DVW-Seminar. Karlsruhe, Schriftenreihe Deutscher Verein für Vermessungswesen, Band 44*, Stuttgart, Germany, 107–116 (in German).
- Wessel, P., W. H. F. Smith, R. Scharroo, J. F. Luis, and F. Wobbe (2013). Generic mapping tools: Improved version released, *EOS Trans. AGU* **94**, 409–410.

J. C. Báez
F. Leyton
C. Troncoso¹
F. del Campo
Centro Sismológico Nacional
Universidad de Chile
Blanco Encalada 2002
Santiago CP 8370449, Chile
jcbaez@csn.uchile.cl
leyton@csn.uchile.cl
ctroncoso@csn.uchile.cl
fdelcampo@csn.uchile.cl

M. Bevis
E. Kendrick
Division of Geodetic Sciences
Ohio State University
125 S. Oval Mall 275 Mendenhall Lab
Columbus, Ohio 43210 U.S.A.
mbevis@osu.edu
kendrick.42@osu.edu

C. Vigny
Laboratoire de Géologie
Ecole Normale Supérieure
24 rue Lhomond
75231 Paris, CEDEX 05
France
vigny@geologie.ens.fr

M. Moreno²
GFZ Helmholtz Centre Potsdam
Telegrafenberg
14473 Potsdam
Germany
marcos@gfz-potsdam.de

M. Simons
Seismological Laboratory
252-21 Caltech
Pasadena, California 91125 U.S.A.
simons@caltech.edu

H. Parra
Instituto Geográfico Militar
Avenida Santa Isabel 1651

Santiago CP 8331014, Chile
sirgas@igm.cl

F. Blume
UNAVCO
6350 Nautilus Drive
Boulder, Colorado 80301 U.S.A.
blume@unavco.org

Published Online 18 April 2018

¹ Also at Universidad Tecnológica de Chile INACAP, Avenida Vitacura 10.151, Santiago CP 8370449, Chile.

² Also at Departamento de Geofísica, Facultad de Ciencias Físicas y Matemáticas, University of Concepción, Víctor Lamas 1290, 4070386 Concepción, Chile.